NR

Norsk Regnesentral
NORWEGIAN COMPUTING CENTER

Note

Leaf Area Index Estimation Using ENVISAT ASAR and Radarsat-2

Note no   **SAMBA/30/09**

Authors   **Arnt-Børre Salberg, Svein Solberg, Dan Johan Weydahl and Rasmus Astrup**

Date   **November 5, 2009**

About the authors

Arnt-Børre Salberg is a Research Scientist in the department for Statistical Analysis, Pattern Recognition and Image Analysis (SAMBA), Earth Observation Group.

Svein Solberg is a Senior Research Scientist at Norwegian Forest and Landscape Institute, P.O. Box 115, N-1431 Ås, Norway.

Dan Johan Weydahl is a Research Scientist at Norwegian Defence Research Establishment (FFI), P.O. Box 25, NO-2027 Kjeller, Norway.

Rasmus Astrup is a Research Scientist at Norwegian Forest and Landscape Institute, P.O. Box 115, N-1431 Ås, Norway.

Norsk Regnesentral

Norsk Regnesentral (Norwegian Computing Center, NR) is a private, independent, non-profit foundation established in 1952. NR carries out contract research and development projects in the areas of information and communication technology and applied statistical modelling. The clients are a broad range of industrial, commercial and public service organizations in the national as well as the international market. Our scientific and technical capabilities are further developed in co-operation with The Research Council of Norway and key customers. The results of our projects may take the form of reports, software, prototypes, and short courses. A proof of the confidence and appreciation our clients have for us is given by the fact that most of our new contracts are signed with previous customers.

Title	**Leaf Area Index Estimation Using ENVISAT ASAR and Radarsat-2**
Authors	**Arnt-Børre Salberg, Svein Solberg, Dan Johan Weydal, and Rasmus Astrup**
Quality assurance	Rune Solberg
Date	November 5
Year	2009
Publication number	SAMBA/30/09

Abstract

In this work we estimate the Leaf Area Index (LAI) using ENVISAT ASAR alternating polarization and Radarsat-2 quad polarization SAR data. The radar backscatter is analysed as a function of LAI to investigate the expected performance, and two different methods are applied for estimating the LAI from radar backscatter. The first is block averaging SAR data, whereas the second method performs averaging of segments with homogeneous LAI values. From the analysis we observed that the HH- and XX-channels saturated for LAI values larger than 1-1.5, but the VV-channel did not. The estimation results clearly shows that Radarsat-2 performs much better LAI estimation than ENVISAT ASAR, and the method based on segment averaging resulted in less noise scatter plots and higher coefficient of determination than the method based on block averaging. Using all polarizations and a quadratic model of the Radarsat-2 data, we obtained as coefficient of determination as high as $R^2 = 0.72$ for segments larger than 144 pixels, but the VV-channel performed nearly as good ($R^2=0.67$). The study shows that satellite based SAR, and in particular Radarsat-2, has the potential for estimating LAI of large areas for small and moderate LAI values.

Contents

List of figures

1 Introduction

The Lear Area Index (LAI) is a dimensionless variable that measures the amount of leaf area per area unit ground surface, and may be used to describe the health of the forest after e.g. a insect attack (e.g. Solberg, 2009)**.** The LAI of a forest area may be accurately described by airborne LIDAR (Solberg, 2009), but surveying large areas with LIDAR is very expensive and time consuming.

To obtain less costly estimates of the LAI we may use data from satellite based sensors. Traditionally, optical methods have been applied to estimate LAI since LAI is the dominant factor behind the spectral reflectance of vegetative canopies in visible and near-infrared radiation. However, optical data has some limitations since it is insensitive to the woody stand structure, which may carry information on LAI, and most important cloud-free daylight conditions are required. For the boreal forest zone, with relatively short summers, acquiring cloud-free optical images may be challenging.

The use of SAR has shown a great potential for obtaining precise estimates of the LAI of boreal forests (Manninen et al., 2005), rice fields (Durden et al. 1995) and corn, sorgum and wheat (Ulaby et al. 1984). Manninen et al. (2005) obtained excellent results using the VV/HH ratio from ENVISAT ASAR data, with a coefficient of determination as high as $R^2=0.78$ for homogeneous forest stands where LAI estimates were obtained using the LAI 2000 instrument. However, even if SAR does not require cloud-free weather conditions, the soil moisture and water content in the vegetation strongly influence the radar backscatter. Zheng et al. (2009) gives an overview of theories, methods and sensors for retrieving LAI using remote sensing

We will in this work analyse the method suggested by Manninen et al. to estimate LAI from both ENVISAT ASAR and Radarsat-2 SAR data on large scale areas, where the ground truth has been obtained by airborne LIDAR. Furthermore, the full polarimetric R2 data will be explored for estimating the LAI, and in particular we investigate the Pauli and Freeman-Durden (Freeman and Durden, 1998) polarimetric decompositions as a means for estimating the LAI. We will not do any model inversion of complex physical models describing the interactions between the radar signal and the forest, but instead focus on empirical models between the radar backscatter and the LAI.

The work also includes a brief analysis of the correspondence between the backscatter and the 0.9 percentile of the height distribution of the LIDAR echoes.

1.1 Acronyms and notation

- HH – horizontal transmit, horizontal receive polarizations.

- VV – vertical transmit, vertical receive polarizations.

- HV - horizontal transmit, vertical receive polarizations.

- VH - vertical transmit, horizontal receive polarizations.

- σ_{pq} : backscatter intensity with transmit polarization p and receive polarization q.

2 Materials

The area of investigation is situated at Palokangas east in Finland, about 62°52'23"N, 30°54'10"E. A Landsat TM image (Aug. 9, 2007) of the scene (Fig. 1) shows that the area is mostly covered by green vegetation.

Figure 1: Landsat TM image (9.aug 2007) of Palokangas, Finland, the area of investigation.

2.1 LIDAR measurements

LIDAR based LAI measurements (Fig. 2) with 10x10m resolution were obtained from aerial surveys. The LAI image was geocoded to ETRS-TM35FIN map coordinate system, but re-defined to UTM35N-WGS84 (in practice the coordinates are the same). The LAI data is not calibrated with respect to field measurements, but gives a good description of how the LAI varies over the area. Also, the factor 1.5 in the equation below has been found to be very constant from scan to scan, because the penetration rate of LIDAR is very stable across LIDAR acquisition settings. The LAI estimates are related to the LIDAR penetration rate (almost equal to the gap fraction) as

$$LAI = 1.5\ln(1/P)$$

where P is the LIDAR penetration rate. Solberg et al. (2009) provides a detailed description on how to estimate LAI from airborne laser measurements.

The 0.9 percentile of the height distribution of the laser echoes were also extracted from the LIDAR data (Fig. 3) and processed to 10x10m resolution. This quantity correlates strongly with the biomass and height of the vegetation, and will be referred to as *PC90*. The LAI and PC90 images are completely different since they are constructed with totally different methods.
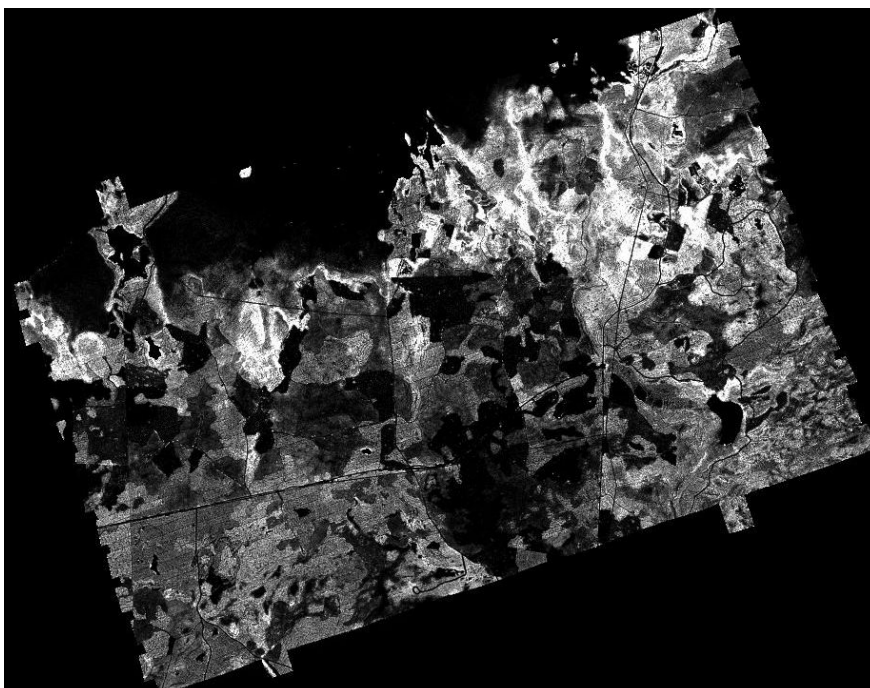
Figure 2: LAI estimated from aerial LIDAR survey. Light areas correspond to high LAI values, and dark areas correspond to low LAI values.
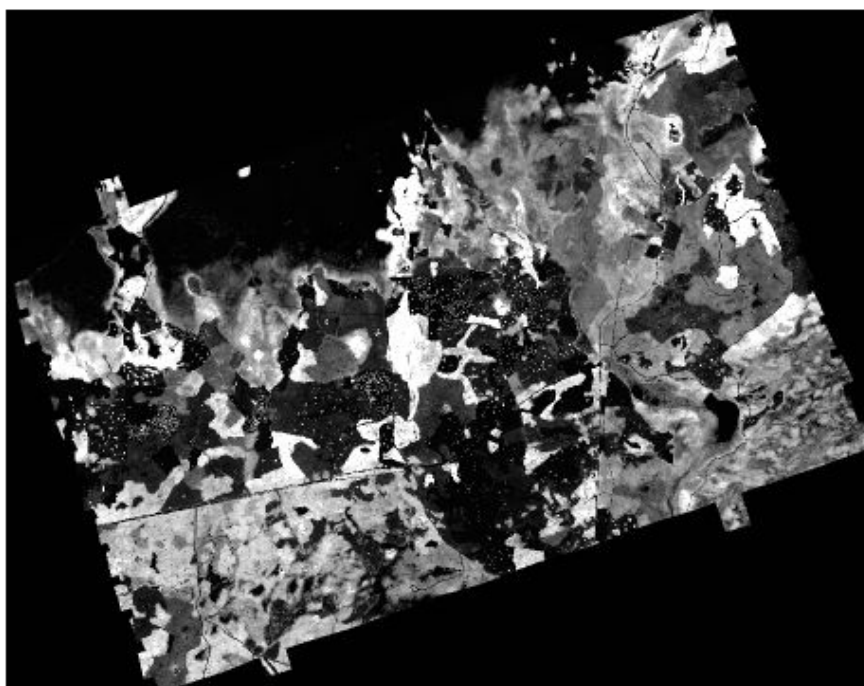
Figure 3; PC90 estimated from aerial LIDAR survey. Light areas correspond to high PC90 values, and dark areas correspond to low PC90 values.

2.2 Homogeneous forest segments

Using the LAI and PC90 measurements the area under investigation was segmented into homogeneous forest segments (Fig. 4) using the software program Defeniens Developer. The borders between the segments were chosen such that the pixels within each segment had low variation of LAI and PC90 values.
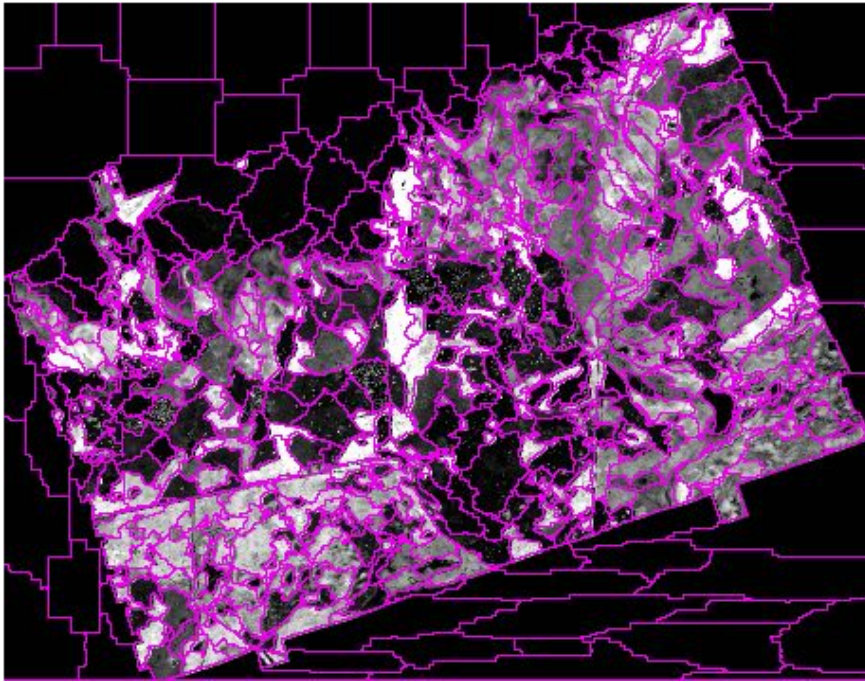
Figure 4: Homogeneous forest segments extracted from the PC90 and LAI data. The background image is the PC90 image.

2.3 ENVISAT ASAR

Three ENVISAT ASAR Alternating Polarization scenes with swat IS7 were acquired from the area under investigation on July 24 (Fig. 5), August 28, and October 2, 2008. The SAR scenes were geocoded to UTM-35 using a digital elevation model (DEM). The scenes were calibrated to σ_0 backscatter values, and the pixel resolution of the geocoded product is 20x20m.

The ENVISAT ASAR Alternating Polarization transmits around 200 pulses (one "burst" period) in one polarization, before it switches the TX and/or RX channels. Every HH and VV image is processed using two burst periods (2-looks).
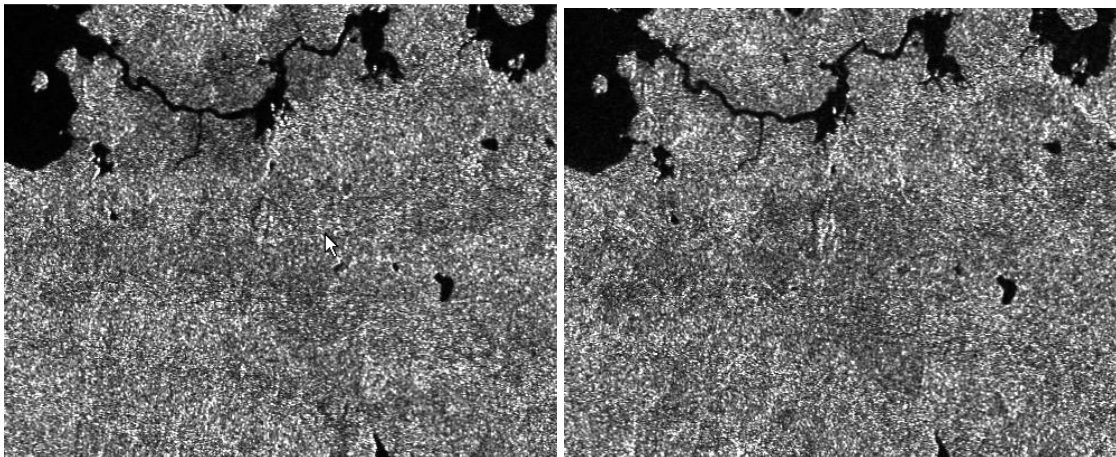
Figure 5: ENVISAT ASAR intensity images of the scene with 20x20m pixel resolution. Left: HH-polarized. Right: VV-polarized.

2.4 Radarsat-II

Three Radarsat-2 Fine-Quad polarization scenes were acquired on July 31, Sept. 3 (Fig. 6), and Sept. 17, 2008. The SAR scenes were also geocoded to UTM-35 using a DEM. The pixel

resolution of the Radarsat-2 scenes were also set to 20x20m in the geocoded product, and radiometrically calibrated to σ_0 values.
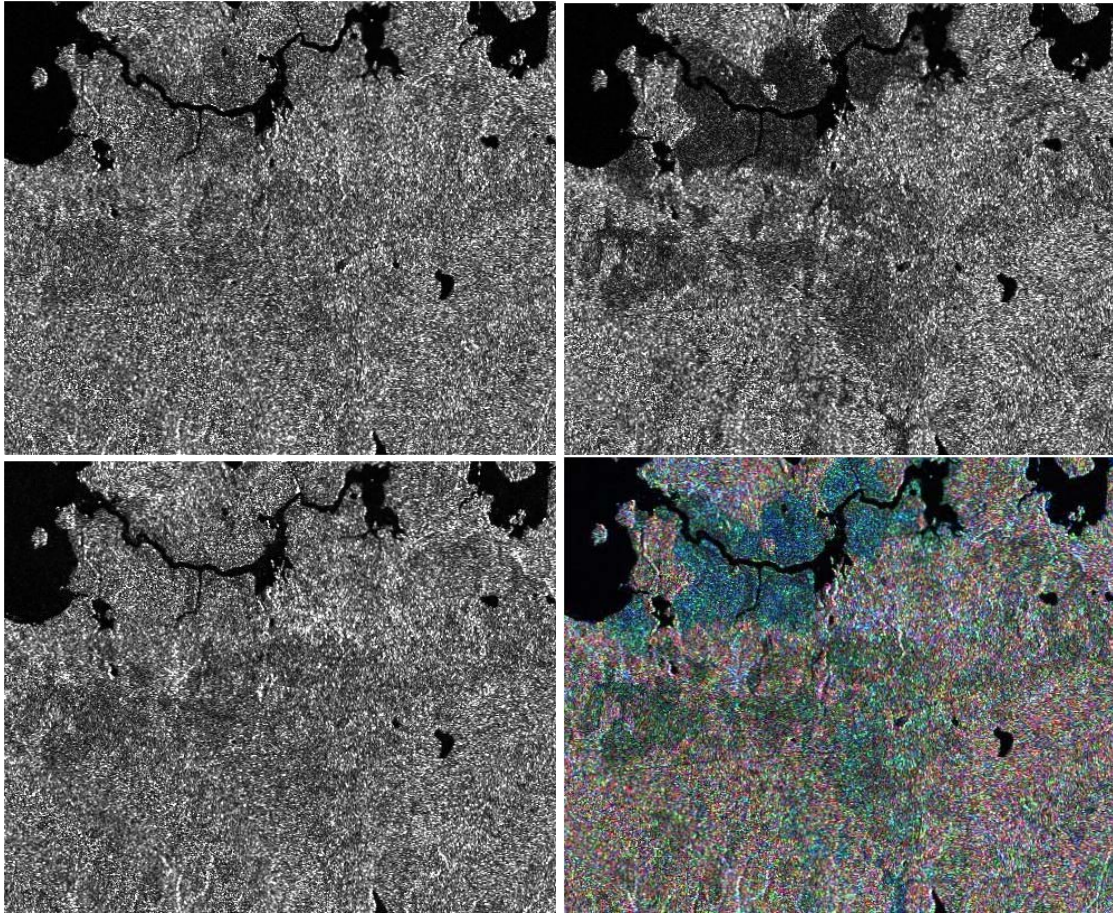
Figure 6: RADARSAT-II intensity images of the scene with 20x20m pixel resolution. Upper/left: HH-polarized. Upper/right: HV-polarized. Lower/left: VV-polarized. Lower-right: Linear decomposition RGB = (HV,HH,VV).

3 Methods

3.1 Geometrical co-registration

Before the SAR images were analyzed with respect to LAI measurements, all images were co-registered to a TerraSAR-X High Resolution Spotlight intensity image (geocoded to UTM-35 using a DEM) with 20x20m pixel resolution.

3.2 Scattering mechanisms
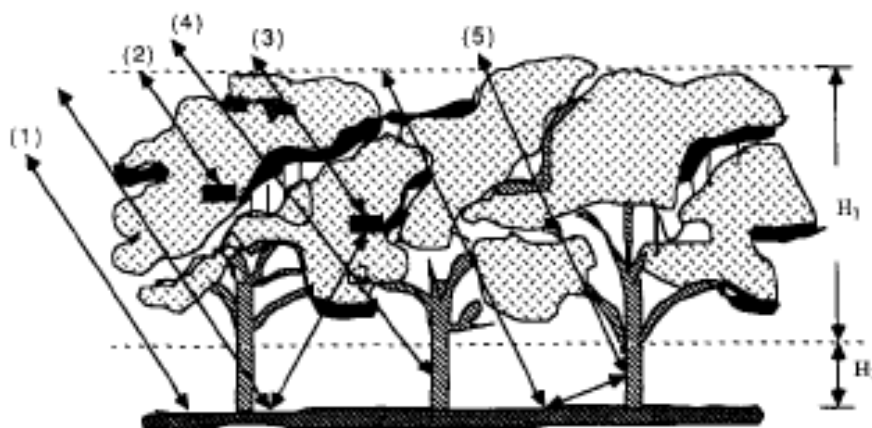
Figure 7: Different types of scatter mechanisms: (1) direct backscattering from the ground, (2) crown scattering including multiple scattering within the crown (crown volume scattering), (3) crown-ground backscatter, (4) direct backscattering from the trunk (usually small), and (5) trunk-ground backscatter (double bounce). The figure taken from Karam et al. (1992).

The total backscatter from forested terrain can include components from several backscatter mechanisms (Fig. 7). These include (1) direct backscattering from the ground, (2) crown scattering including multiple scattering within the crown (crown volume scattering), (3) crown-ground backscatter, (4) direct backscattering from the trunk (usually small), and (5) trunk-ground backscatter (double bounce). The crown-ground and trunk-ground bounces can be in both directions from tree to ground or ground to tree. Volume scattering is relevant to backscatter from a vegetation canopy. The main elements within a forest canopy are leaves, twigs, branches and trunks. There are many such elements acting as scatters and resulting in multiple scattering between elements, but also acting as attenuators. Of course, backscatter from beneath the canopy will often be attenuated by the canopy as it travels back towards the satellite. In cases where there is interaction with the ground, factors such as surface roughness, soil moisture, and slope has important influence. In addition, there is often an understory or layer of ground vegetation that may strongly influence the backscatter interactions (Leckie and Ranson, 1998).

The magnitude of each one of these backscatter components depends on radar wavelength, polarization, angle of incidence and a myriad of terrain and canopy parameters. A convenient simplification of the interaction between tree elements and different radar wavelengths is that K-band primarily interact with leaves, X-band with leaves, twigs and small branches, C-band with the leaves, and small and secondary branches, L-band with the primary and secondary branches and trunks, including some interaction with the ground, and P-band interacts mostly with the main branches, trunks and ground. Trunk-ground and crown-ground interactions can be important for L- and P-band (Leckie and Ranson, 1998).

3.2.1 Polarimetry

Radar polarimetry is a technique that provides many options for analysis and understanding of radar backscatter from forest terrain. The Stokes vector collects four parameters that allow a complete description of a polarized wave may be expressed as

$$\mathbf{g} = \begin{bmatrix} \langle E_V^2 \rangle + \langle E_H^2 \rangle \\ \langle E_V^2 \rangle - \langle E_H^2 \rangle \\ 2\,\mathrm{Re}\left\{ \langle E_V E_H^* \rangle \right\} \\ 2\,\mathrm{Im}\left\{ \langle E_V E_H^* \rangle \right\} \end{bmatrix}$$

where the <…> brackets denote averaging over time. The first element is a measure of the total amount of power in the wave, and the three last terms describe the state of the polarization. A polarized wave represented by Stokes vector g_i that interacts with a target, and results in a wave represented by the vector g_s. The scattering process transform one vector, g_i, into another vector g_s, a process that can be described using a 4x4 real matrix M, as

$$\mathbf{g}_s = \mathbf{M}\mathbf{g}_i$$

The matrix M is called *Stokes scattering matrix or Mueller matrix*. Each term of the Stokes matrix has a physical significance related to total power, fraction of like-polarized power, difference between HH and VV power, or the nature of depolarization. This matrix operator therefore contains the information we are looking for with regard to the target's effect on a polarized wave, since it completely describes the polarimetric response of the target (Woodhouse, 2006; Leckie and Ranson, 1998).

For radar polarimetry, the Stokes vector is not the most effective way to characterize the data since there are effectively two measurements of polarization to quantify—one for each of the orthogonal transmitted pulses. The radar system transmits a horizontal signal, measures the echo polarization, transmits a vertical polarized wave and measures the polarization of that echo. At least two Stokes vectors would then be required (Woodhouse, 2006). Since the polarimetric measurements of the echoes are made as orthogonal measurements it is convenient to define an alternative scattering matrix

$$\mathbf{S} = \begin{bmatrix} S_{VV} & S_{VH} \\ S_{HV} & S_{HH} \end{bmatrix}$$

which describes the relationship between incident and scattered wave fields, rather than Stokes vectors. Once reciprocity, $S_{VH} = S_{HV}$, has been assumed the elements of S may be stacked into a 3 element vector $k = [S_{VV},\ S_{HV},\ S_{HH}]^T$. The linear basis is not always the most efficient way of dealing with the analysis of polarimetric data, and the *Pauli basis* of the target vector

$$\mathbf{k}_P = \left[S_{HH} - S_{VV}, 2S_{HV}, S_{HH} + S_{VV}, \right]^T$$

is for many applications more useful as it helps to emphasise the phase difference between the HH and VV terms. Double-interactions are dominated by the first term, multiple (volume) scattering dominates the second term, and direct scattering is dominated by the second term (Fig. 8).
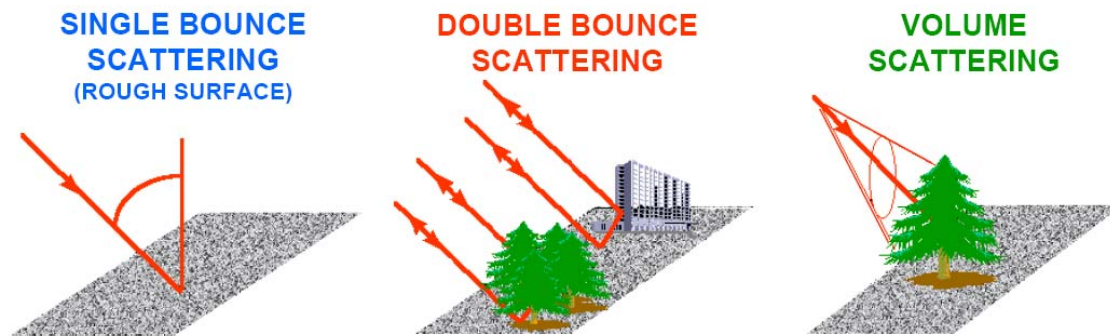
Figure 8: Different types of scattering mechanisms involved.

3.3 Analysis of the SAR scenes

We now briefly summarize how the physical radar backscatter may be modelled, and suggest empirical models to estimate the LAI and PC90 from measured backscatter intensity values.

3.3.1 Physical backscatter modelling

Radar backscatter models are important for understanding the various influences on backscatter, to interpret the imagery, and to estimate biophysical parameters from the imagery using model inversion techniques. Crown scatters is considered as volume scattering, and is usually modelled as scattering from randomly distributed, unconnected, simple characterization of the canopy elements (discrete approach), or as a collection of point scatters acting similar to water droplets (the water cloud model) (e.g., Ulaby et al. 1984). Distributions of dielectric disks or cylinders representing leafs, branches or needles have been used (Durden et al., 1989). The MIMICS model by Ulaby et al.(1990) represented needles and braches as dielectric cylinders and leaves as dielectric rectangles. Within the canopy most models only incorporate single scattering events. Ground reflections are often modelled as rough-surface scatter, and trunks are generally modelled as lossy dielectric (i.e. conduction current is not negligible) cylinders with smooth surfaces (being a smooth surface there is no direct backscatter, and the only important influence is the ground-trunk double-bounce). Crown-ground double bounce is also incorporated into many models, but is considered as a smaller than direct canopy and trunk-ground backscatter.

Many physical models solve the "forward problem" in predicting the backscatter form a number of ground-based measurements of the imaged objects. It is difficult, if not impossible, to invert these models to provide unique solutions for LAI or PC90, since the number of parameters describing the "ground truth" is often much larger than then number of radar measurements in the forward problem (Freeman and Durden, 1998). Even the simple models for backscatter as a function of LAI given by Durden et al. (1995) and Ulaby et al. (1984), is not easy to invert.

A useful decomposition of polarimetric radar data is the Freeman-Durden decomposition (Freeman and Durden, 1998), which is a method for fitting three simple scattering mechanisms to polarimetric SAR observations. The mechanisms are canopy scatter from a cloud of randomly oriented dipoles, even- or double-bounce scatter from a pair of orthogonal surfaces with different dielectric constants and Bragg scatter from a moderately rough surface. The method allows for decomposing the power forms of the scattering matrix so that the amount of odd-bounce (surface), even-bounce (double bounce) and volume scattering from each averaged group of samples can be estimated.

3.3.2 Empirical models

Manninen et al. (2005) showed that LAI of Norway spruce and Scots pine were well explained by the backscattering ratio VV/HH of ENVISAT ASAR Alternating-polarization (IS1-IS6) when the LAI and ASAR are integrated to a pixel resolution of about 270x270m and using a weighted and truncated mean (the highest 25% and lowest 25% intensity values were excluded). In their study they obtain a coefficient of determination from the linear model

$$L\hat{A}I = a_0 + a_1(\sigma_{VV} / \sigma_{HH})$$

as high as $R^2=0.78$ from a single image and with a percentage of deciduous species less than 10%. However, it should be noted that the dynamical VV/HH ratio in their study had a limited range from 0.9 to 1.2! Manninen et al. (2005) also considered estimating the LAI from multiple images. This may be achieved using the linear model

$$L\hat{A}I = a + b_1(\sigma_{VV1} / \sigma_{HH1}) + ... + b_K(\sigma_{VVK} / \sigma_{HHK}),$$

where the subscript refers to image number.

We will in our study of the SAR images also apply the methods suggested by Manninen et al. (2005). In addition, we investigate the relationship between LAI and the polarization channels (HH, XX and VV), or a transformation of them, separately.

We consider three different methods of comparing the SAR backscatter values with the LAI measurements:

1. In Method 1 we simply block average the LAI image and the radar backscatter intensity image, ignoring that the LAI values may vary within a block. The estimate of the average backscatter values was obtained using a truncated mean, i.e. the lowest and highest α% values were ignored.
2. *In Method 2 we rank (sort) the pixel values of the LAI image, and store the corresponding set of indices. We then divide the sorted LAI values into segments of M values, and compute the average of each segment and of the radar backscatter values corresponding to the indices of each segment of sorted LAI values. Thus, we estimate the average of radar backscatter values for indices where the LAI estimates are close in value. Please note that this method is only suitable for analysis of the relationship between LAI and radar backscatter, and not suitable for predicting the LAI from a given SAR image.*
3. In Method 3 we average the LAI image and the radar backscatter intensity images according to the defined segments shown in Fig. 4. The estimate of the average backscatter values was obtained using a truncated mean, i.e. the lowest and highest α% values were ignored.

By block averaging we refer to dividing the image into blocks of *MxM* pixels, and compute the (truncated) mean within each block. Note that by setting *M*=1for Method 1 we compute the pixel correspondence between the LAI image and the corresponding radar backscatter.

Analyses based on Method 3 are also performed on the PC90 image.

A "forward" model represent the backscatter for a given polarization *pq* as a non-linear function of LAI (Durden et al., 1995, Ulaby et al., 1984)

$$\sigma_{pq} \equiv f(LAI)$$

Now, if we have *N* corresponding LAI and radar backscatter measurements, it is important to note that

$$\frac{1}{N}\sum_{k=1}^{N}\sigma_{pq}^{k} \equiv \frac{1}{N}\sum_{k=1}^{N}f(LAI_k) \neq f\left(\overline{LAI}\right)$$

where

$$\overline{LAI} = \frac{1}{N}\sum_{k=1}^{N}LAI_k$$

Hence, the relationship between the radar backscatter and LAI does not hold when we consider average values. The inverse function $LAI = f^{-1}\left(\sigma_{pq}\right)$ is not easy to obtain, and we therefore propose to model the LAI from backscatter values using a simple quadratic model

$$L\hat{A}I = a_0 + a_1\sigma_{HH} + a_2\sigma_{HH}^2 + a_3\sigma_{XX} + a_4\sigma_{XX}^2 + a_5\sigma_{VV} + a_6\sigma_{VV}^2$$

where σ_{HH}, σ_{VV} and σ_{XX} denote the backscatter with horizontal, vertical and cross polarization, respectively. When estimating LAI from ENVISAT ASAR the cross polarization terms are of course not included.

Least squares are applied to estimate the unknown parameters, and the fit is evaluated using the coefficient of determination defined as

$$R^2 = 1 - \frac{n}{n-p} \cdot \frac{\sum_{i=1}^{n}(LAI_i - L\hat{A}I_i)^2}{\sum_{i=1}^{n}(LAI_i - \overline{LAI})^2}$$

where *n* is the number of observations and *p* is the number of model parameters.

For Radarsat-2 scenes we also apply the analysis suggest above on Pauli and Freeman-Durden decompositions to investigate the radar signal backscatter mechanism, i.e. we model the LAI as

$$L\hat{A}I = a_0 + a_1 P_1 + a_2 P_1^2 + a_3 P_2 + a_4 P_2^2 + a_5 P_3 + a_6 P_3^2$$

where (P1,P2, P3) =(HH-VV, HV+VH, HH+VV) in the case of Pauli components. A similar model is also applied to the Freeman-Durden components as well.

Note that the radar data may be analysed similarly with respect to the PC90 data.

4 Results

For all scenes the block size for Method 1 was 12x12 pixels and the segment size was 144 samples for Method 2 (if other values are not specified), and the α-value used in the truncated mean computations was 0.1. Estimated LAI values smaller than 0 was set equal to zero.

4.1 ENVISAT ASAR

Clearly, at 20x20m resolution, both HH- and VV-polarized images contain a large amount of speckle noise (Fig. 5). Hence, we need to increase the number of looks using Method 1, 2 or 3 before we analyse the images with respect to the LAI image.

For the ENVISAT ASAR data we present various scatter plots between for the Aug. 28 scene, and summarized the results for all other ENVISAT ASAR scenes (Tab. 1). Method 3 was also applied to estimate the PC90 for the radar backscatter (Tab. 2).

4.1.1 LAI modelling and prediction

Using Method 2 we compared the LAI image with the SAR image, and observed that for both HH and VV channels the backscatter intensity was increasing for increasing values of the LAI (Fig. 9). Note that for the HH channel the backscatter saturated for LAI values higher than 1, whereas there was only a weak trend against LAI for VV backscatter intensity values larger than 1.

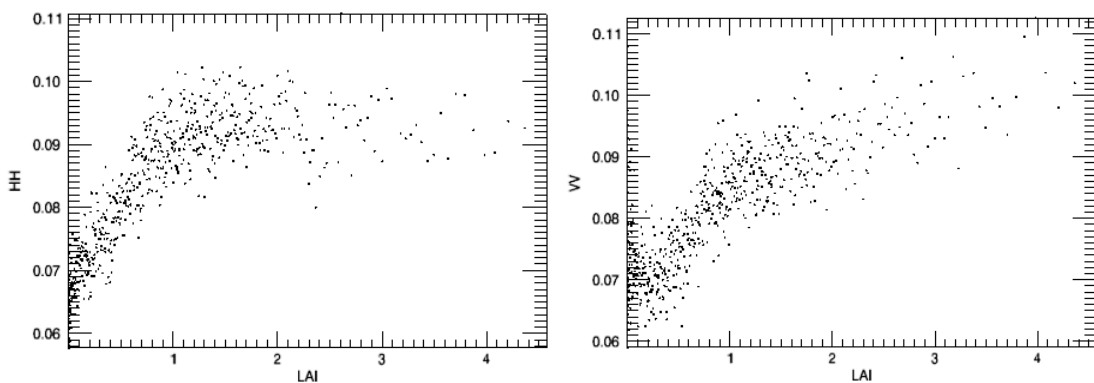Figure 9: LAI versus backscatter using Method 2 for ENVISAT ASAR (Aug. 28, 2008). Left panel: HH-polarization. Right panel: VV-polarization.

Using Method 1 we compared LAI and backscatter HH and VV and obtained noisy scatter plots for backscatter versus LAI (Fig. 10). The coefficient of determination for HH and VV backscatter using linear regression were as low as $R^2=0.26$ (MSE=0.31) and $R^2=0.22$ (MSE=0.33), respectively.
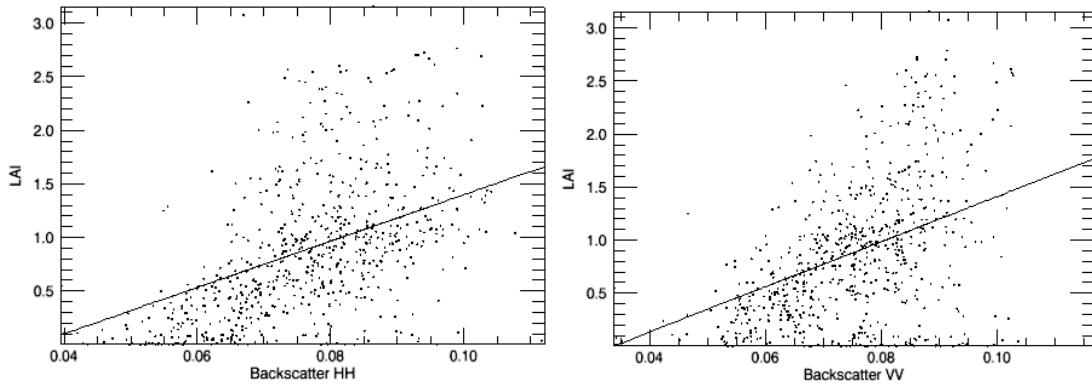
Figure 10: LAI versus backscatter HH (right) and VV (left) using Method 1 for ENVISAT ASAR (Aug. 28, 2008). The coefficient of determination is as $R^2=0.26$ and $R^2=0.22$ for HH and VV backscatter, respectively.

When we used Method 3 to estimate the LAI from backscatter HH and VV the scatter plots were slightly less noisier (Fig. 11), and we obtained coefficients of determination for HH and VV equal to $R^2=0.29$ (MSE=0.33) and $R^2=0.39$ (MSE=0.28), respectively.
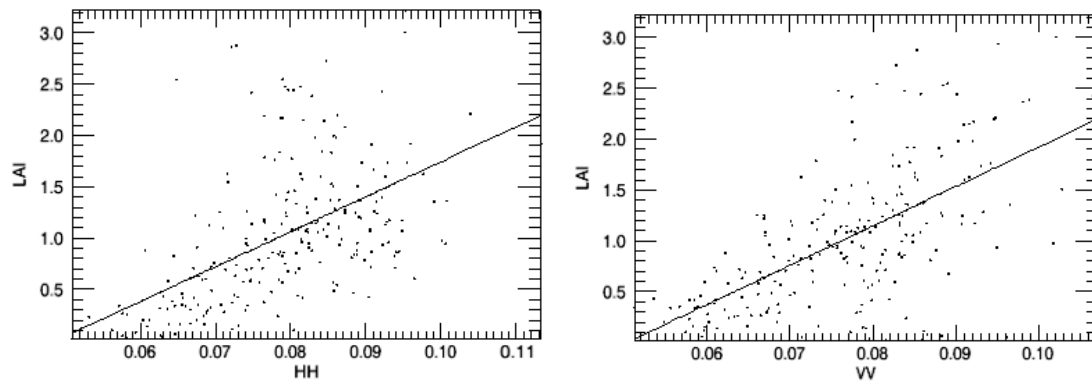
Figure 11: LAI versus backscatter HH (right) and VV (left) using Method 3 for ENVISAT ASAR (Aug. 28, 2008). The coefficient of determination is as $R^2=0.29$ and $R^2=0.39$ for HH and VV backscatter, respectively

The Manninen et al. (2005) approach was also evaluated, and fig. 12 shows the scatter plots between LAI and the VV/HH backscatter ratio using Method 1 (left) and Method 3 (right). There seemed to be no correlation between the quantities, and the resulting coefficient of determination for Method 1 (left) and Method 3 (right) when modelling using linear regression is only $R^2=0.09$ (MSE=0.22) using Method 1. For Method 3 we obtained $R^2=0$ (MSE=0.46). The noisiness of the scatter plots resulted in a negative linear trend between the backscatter and LAI for Method 1 and only a weak positive trend for Method 3.

Figure 12: Dependence of measured LAI on the VV/HH backscattering ratio using Method 1 (left) and Method 3 (right) of the ASAR image of Aug. 28, 2008.

The best prediction of LAI from the ENVISAT ASAR images was on the average of the images of Aug. 28 and Oct. 2, 2008 (Fig. 13) and the suggested quadratic model. The coefficient of determination for Method 1(left) and Method 3 (right) were 0.38 (MSE=0.26) and 0.49 (MSE=0.23), respectively.
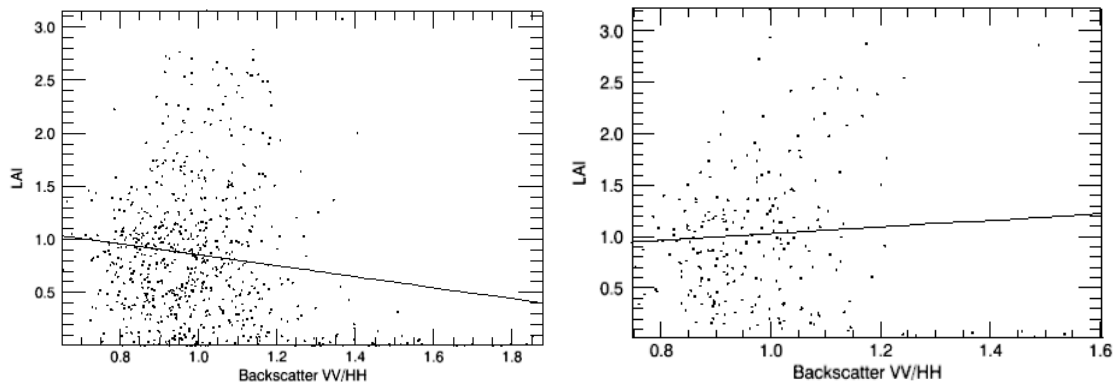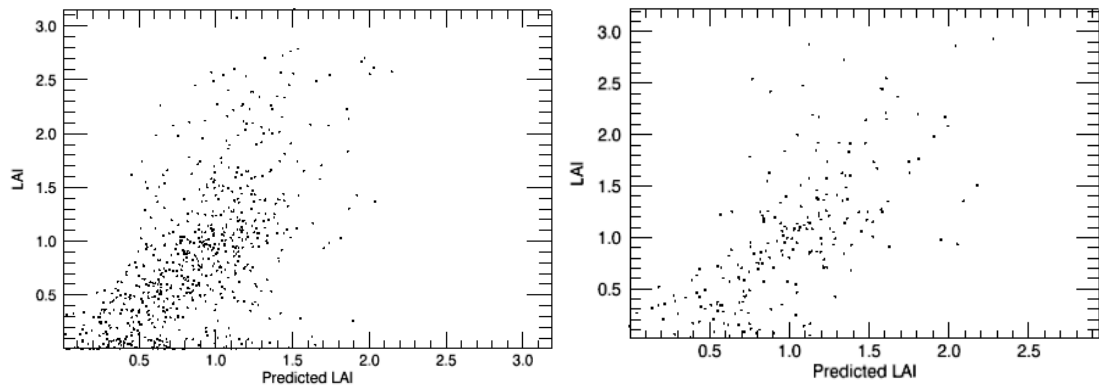

Figure 13: LAI versus predicted LAI Method 1 (left) and Method 3 (right) on the average of ASAR images of Aug 28 and Oct. 2, 2008. The coefficient of determination were $R^2=0.38$ and $R^2=0.45$.

The results for the July 24 and Oct. 2 scenes were worse than for the Aug. 28 scene (Tab. 1). Increasing the number of samples in each LAI cell (288 samples) did not improve the estimation results (Tab. 1). For HH the R^2 increased to 0.39, but for the VV channel the R^2 decreased to 0.16. The PC90 data correlated a little higher for the HH-channel ($R^2=0.39$), and little less for the VV-channel ($R^2=0.23$) (Tab. 2).

4.1.2   Summary LAI estimation using ENVISAT ASAR

Table 1: Summary of LAI estimation results using ENVISAT ASAR.

Scene	Model	Method 1		Method 3	
		R-sq	MSE	R-sq	MSE
ASAR – Aug, 28	a0 + a1*HH	0.26	0.31	0.29	0.33

	a0 + a1*VV	0.22	0.33	0.39	0.28
	a0 + a1*(VV/HH)	0.09	0.22	0	0.36
ASAR – Oct., 2	a0 + a1*HH	0.18	0.35	0.14	0.39
	a0 + a1*VV	0.19	0.34	0.30	0.32
ASAR – July, 24	a0 + a1*HH	0.21	0.33	0.22	0.36
	a0 + a1*VV	0.22	0.33	0.32	0.32
ASAR – Aug., 28 + Oct., 2	a0 + a1*HH + a2*HH^2 + a3*VV +a4*VV^2	0.38	0.26	0.49	0.23
ASAR – Aug, 28 288 samples	a0 + a1*HH	0.28	0.24	0.37	0.19
	a0 + a1*VV	0.25	0.26	0.15	0.26

4.1.3   Summary PC90 estimation using ENVISAT ASAR

Table 2: Summary of PC90 estimation results using ENVISAT ASAR.

Scene	Model	Method 3	
		R-sq	MSE
ASAR – Aug, 28	a0 + a1*HH	0.35	12.2
	a0 + a1*VV	0.23	14.5
ASAR – Aug., 28 + Oct., 2	a0 + a1*HH + a2*HH^2 + a3*VV +a4*VV^2	0.43	10.3

4.2 RADARSAT-II

The Radarsat-2 images seem to contain more information about the ground cover type, than the ENVISAT ASAR images. In particular, the cross-polarized bands HV (and VH) show spatial clustering of the intensity values (Fig. 6(a-c)). A colour image constructed using the linear decomposition RGB = (σ_{HH}, σ_{XX} , σ_{VV}) further enhances the observed spatial clustering of the data (Fig. 6(d)). Comparing this image with the Landsat image (Fig. 1) we see that the different colours tend to correspond to different vegetation types.

For the Radarsat-2 data we present various scatter plots between for the Sept. 3 scene, and summarized the results for all other ENVISAT ASAR scenes (Tab. 3). Method 3 was also applied to estimate the PC90 for the radar backscatter (Tab. 4).

4.2.1   LAI modelling and estimation

Using Method 2 we compared the LAI image with the Radarsat-2 backscatter, and we observed that for the HH- and VV-channels the backscatter intensity were increasing for increasing values of LAI less than 1.5 (Fig. 14). The backscatter saturated for LAI values higher than 1.5. For the VV-channel the backscatter intensity was increasing for increasing values of LAI, but the slope was higher for LAI values less than 1.5.

The backscatter intensity components (HH, XX, and VV) for the Sep. 3 scene were also evaluated against LAI using Method 1 and Method 3 (Fig. 15). The coefficients of determination using Method 1 (Fig. 15, left panels) where R^2=0.50 (MSE=0.21), 0.44 (MSE=0.23) and 0.50 (MSE=0.21) for HH, XX and VV, respectively, and for Method 3 (Fig. 15, right panels) R^2=0.60 (MSE=0.18), 0.50 (MSE=0.22) and 0.67 (MSE=0.15). Hence, by using Method 3 we obtained a stronger correspondence between LAI and radar backscatter with the VV-channel as the most predictive.
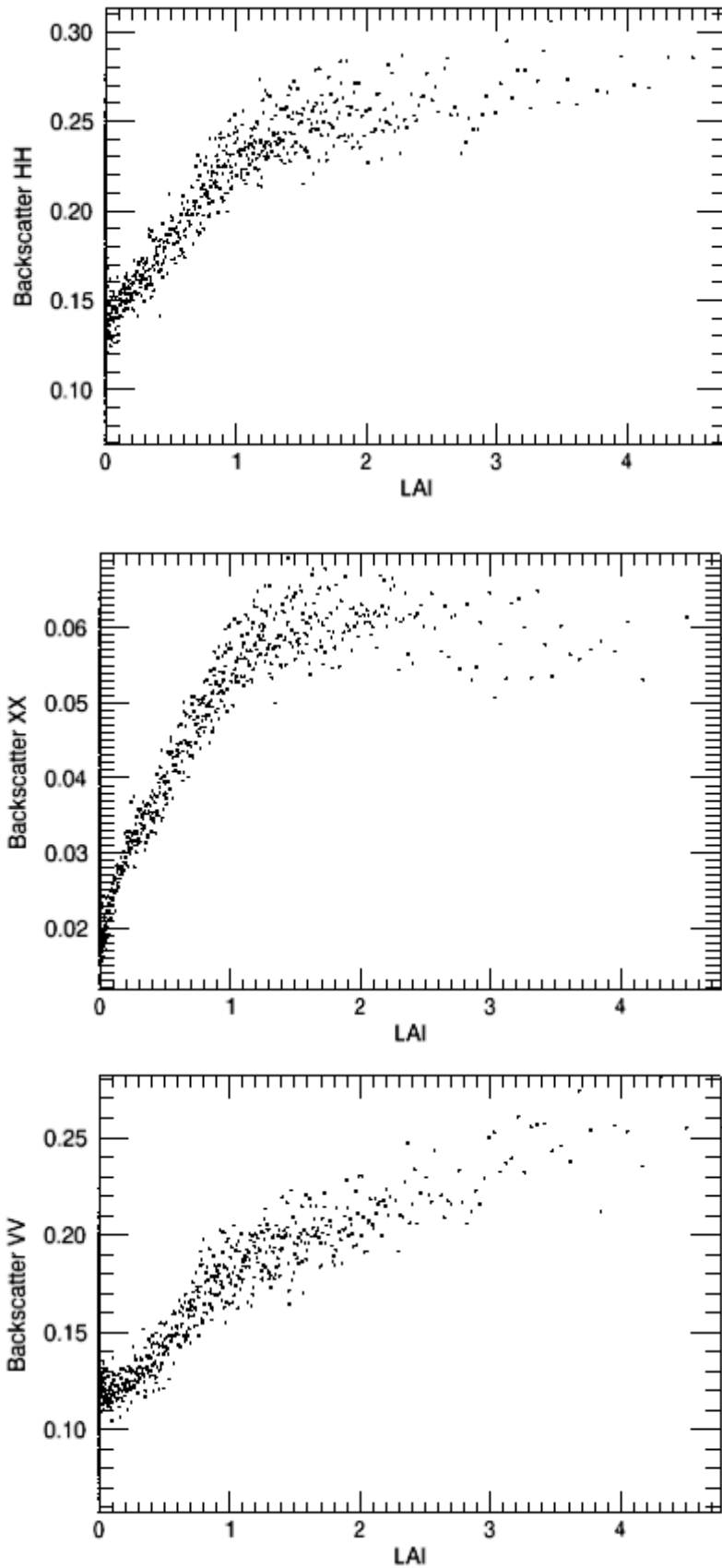
Figure 14: LAI versus HH (upper), XX (middle), VV (lower) using Method 2 for Radarsat-2 (Sept. 3, 2008).
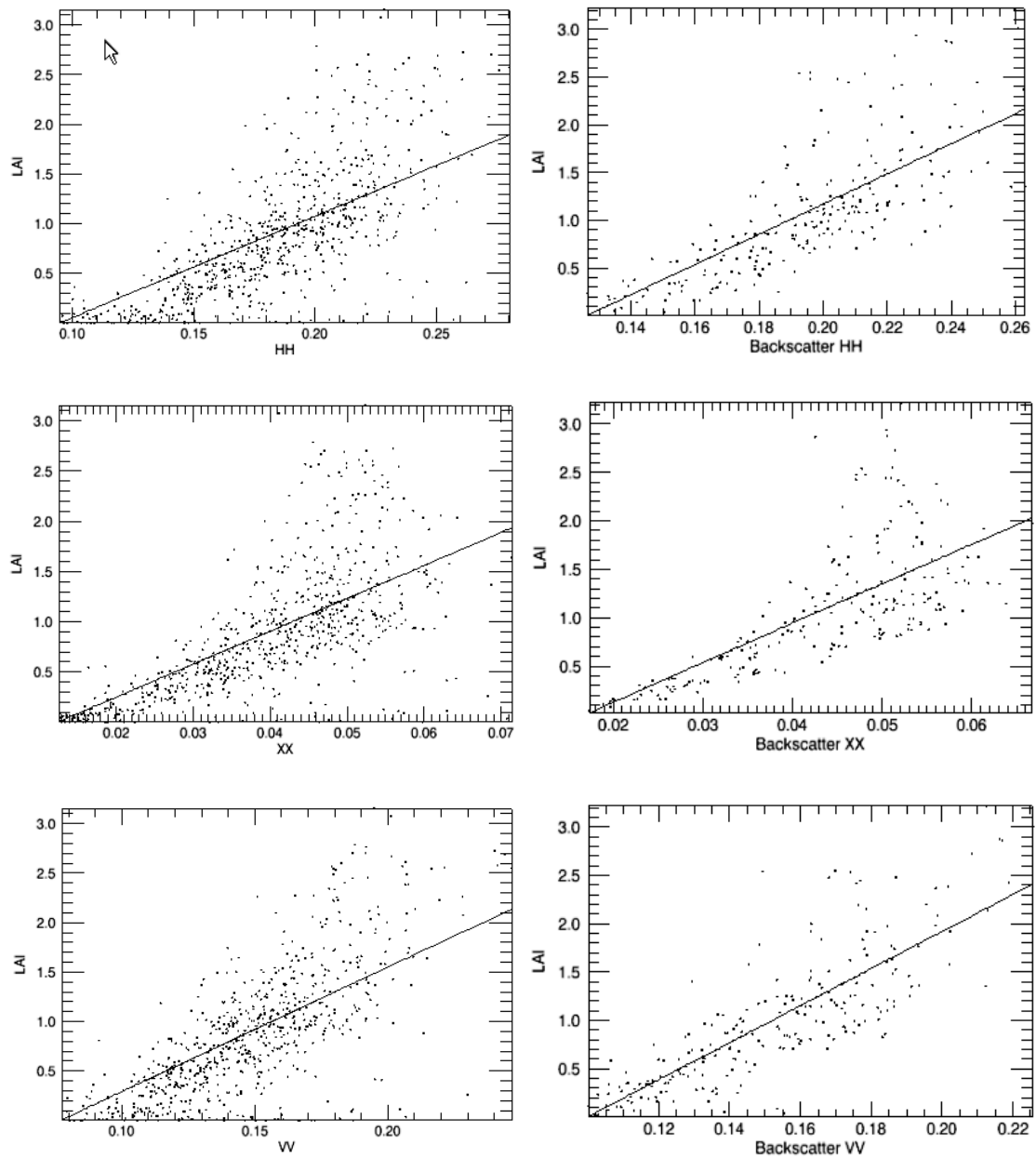
Figure 15: Dependence of measured LAI on the HH (upper panels), XX (mid panels) and VV (lower panels) backscatter using Method 1 (left) and Method 3 (right) on the R2 Sept., 3, 2008 scene.

The best predictions of the LAI from the Radarsat-2 images were obtained on the Sept. 3, 2008 scene and using the quadratic model (Fig. 16). The coefficient of determination using Method 1 (left) and Method 3 (right) were 0.60 (MSE=0.17) and 0.72 (MSE=0.12), respectively. The increase in R^2 from the VV-channel only was only modest.

Figure 16: LAI versus predicted LAI using Method 1 (left) and Method 3 (right) on the R2 image of Sept. 3, 2008. The coefficients of determination are R^2=0.60 and R^2=0.72, respectively.

4.2.1.1 Pauli decomposition

The vegetation pattern shown in the Landsat image (Fig. 1) was even more revealed by the Pauli decomposition image (Fig. 6). Please note that this image has a 20x20m resolution!
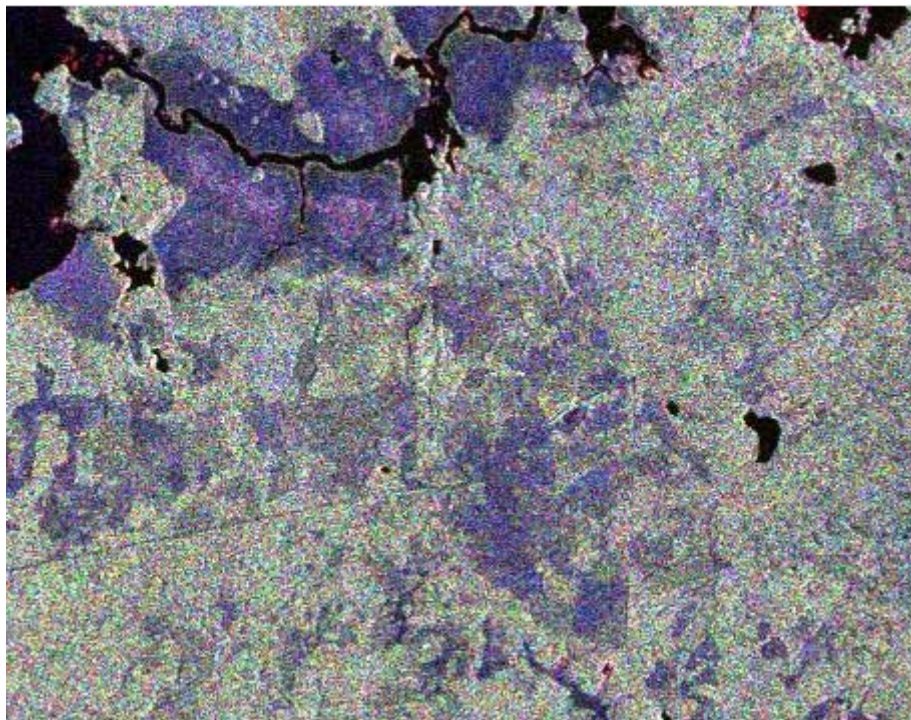
Figure 17: Color image created from the Pauli decompositions of the R-2 Sept. 3, 2008 scene. The colours are encoded as (RED, GREEN, BLUE) = (DOUBLE, VOLUME, SINGLE).
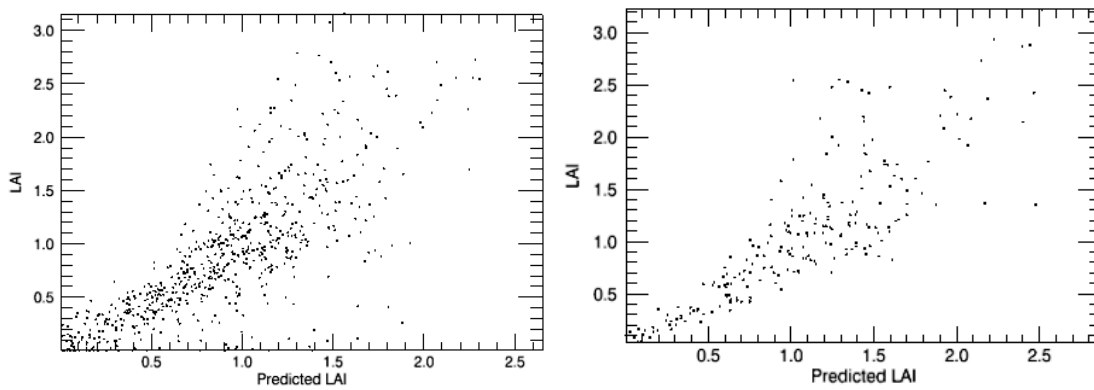
The relationship between the Pauli components of the Radarsat-2 image of Sept. 3, 2008 versus LAI using Method 2 showed similar patterns as for the individual backscatter intensity (HH, XX and VV) components (Fig. 18). The first (double bounce) and second (volume) components showed a clear non-linear trend against the LAI, whereas the third (single-bounce) component showed more or less no trend against the LAI. As for the individual HH and XX backscatter components the two first Pauli components saturated for LAI values greater than 1.
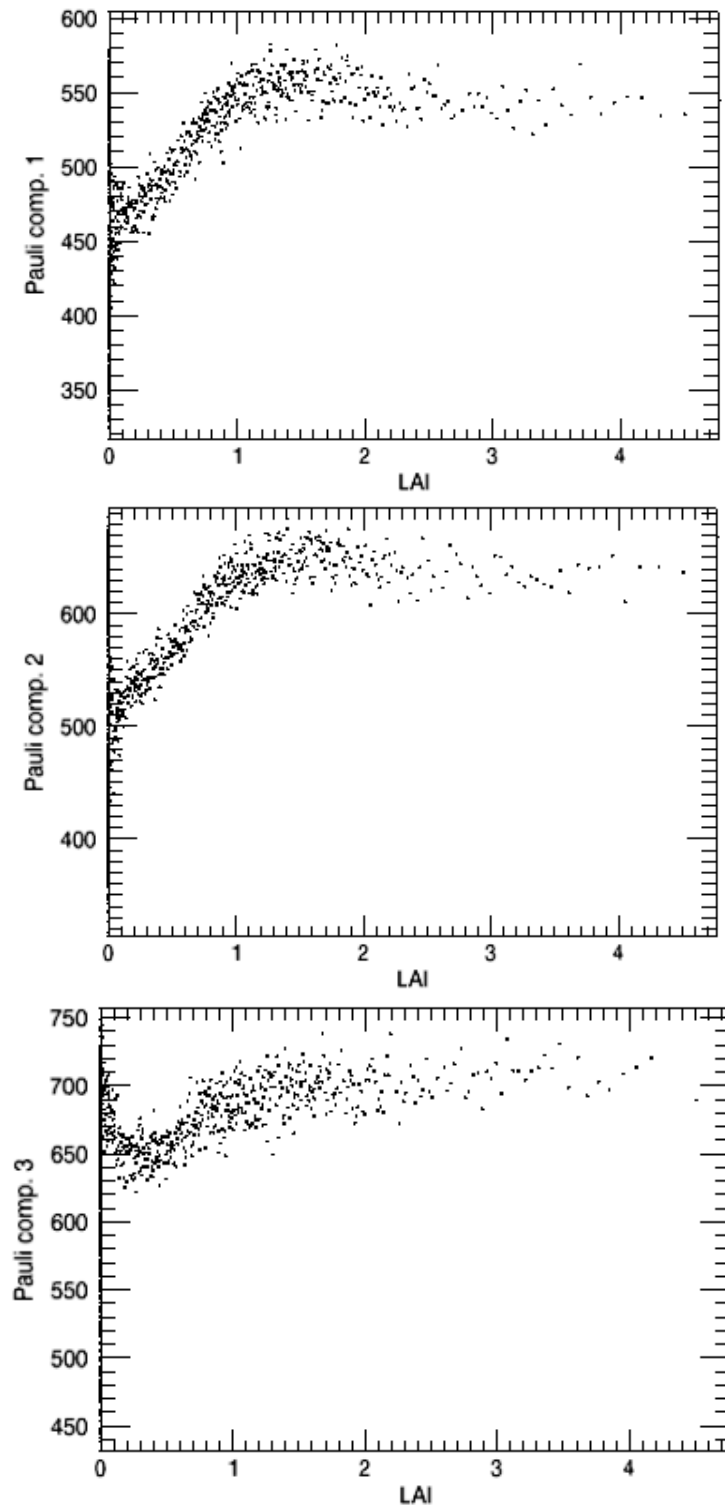
Figure 18: LAI versus Pauli components (Sept. 3, 2008) using Method 2..

The Pauli components were also evaluated against LAI using Method 1 and Method 3 and showed a clear correspondence against LAI (Fig. 19). The coefficients of determination were using Method 1 (Fig. 19, left panels) R^2=0.39 (MSE=0.25), 0.41 (MSE=0.25) and 0.33 (MSE=0.28)

for Pauli component 1, 2, and 3, respectively, and for Method 3 (Fig. 19, right panels) R^2=0.44 (MSE=0.25), 0.48 (MSE=0.23) and 0.59 (MSE=0.19).
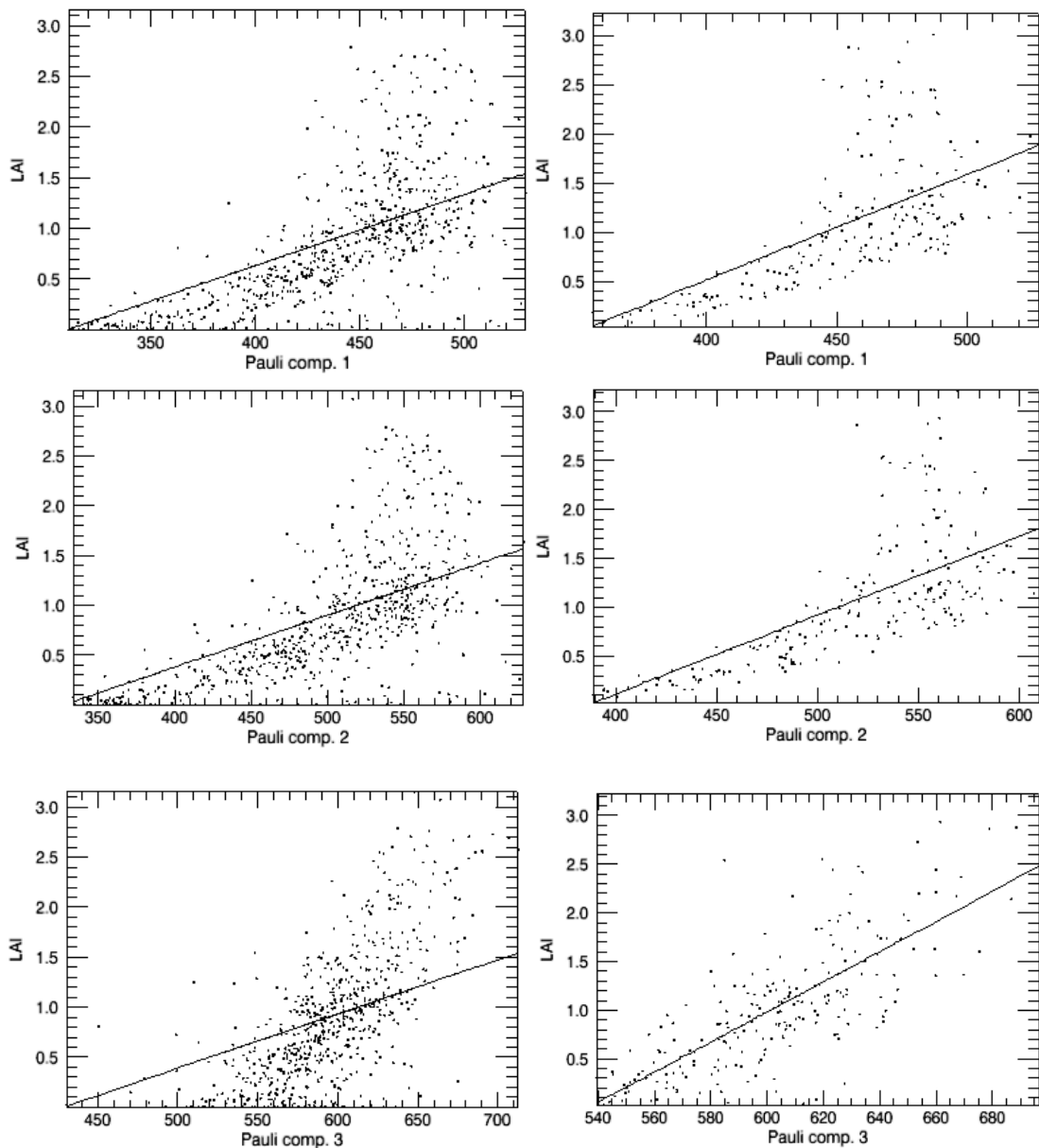
Figure 19: Dependence of measured LAI on the Pauli components using Method 1 (left) and Method 3 (right) on the R2 Sept., 3, 2008 scene.

The best predictions of the LAI from the Pauli components were obtained on the Sept. 3, 2008 scene and using the quadratic model (Fig. 20). The coefficient of determination using Method 1 (left) and Method 3 (right) were 0.56 (MSE=0.18) and 0.70 (MSE=0.13), respectively. Hence, the correspondence against LAI was almost equal as for the individual backscatter channels (Fig. 16).
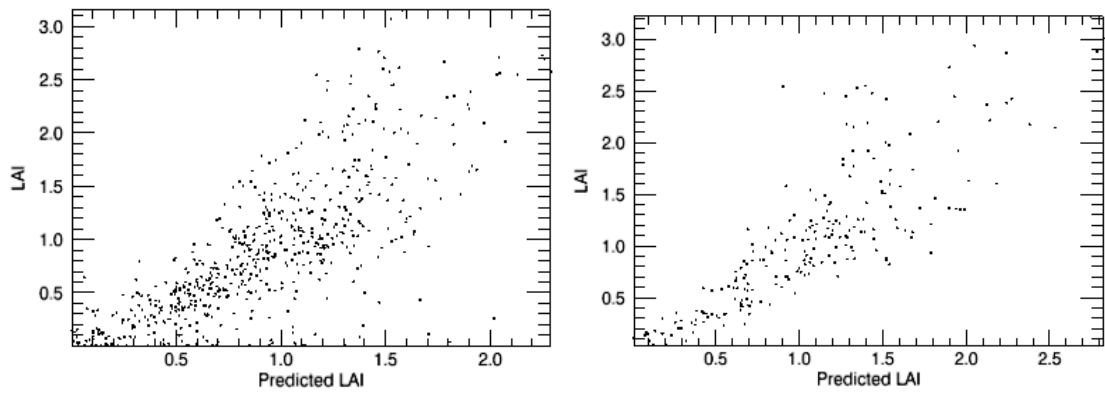
Figure 20: LAI versus predicted LAI using Method 1 (left) and Method 3 (right) on the R2 image of Sept. 3, 2008. The coefficients of determination are $R^2=0.56$ and $R^2=0.70$, respectively.

4.2.1.2 Freeman-Durden decomposition

Lee filtered Freeman-Durden components of the Radarsat-2 image of Sept. 3, 2008 versus LAI were evaluated using Method 2, and the first (double bounce) and second (volume) components show a clear non-linear trend against the LAI (Fig. 21, upper and mid panel) and saturated for LAI values greater than 1.5. The third (single-bounce) component showed an almost linear trend against the LAI (Fig. 21, lower panel). We also observed that due to the Lee speckle filter the scatter plots are less nosy than Figs. 14 and 18.

The results using Method 1 and Method 3 and the quadratic model on Freeman-Durden decompositions showed, as expected, a clear relationship between LAI and the predicted LAI (Fig. 22). The obtained coefficient of determination were R^2=0.58 (MSE=0,17) and 0.70 (MSE=0.13), respectively, which was similar to the results obtained with the individual backscatter channels and the Pauli components.

Figure 21: LAI versus Freeman-Durden components (Sept. 3, 2008) using Method 2. Upper panel: Double bounce component. Mid panel: Volume scattering component. Lower panel: Single bounce component..
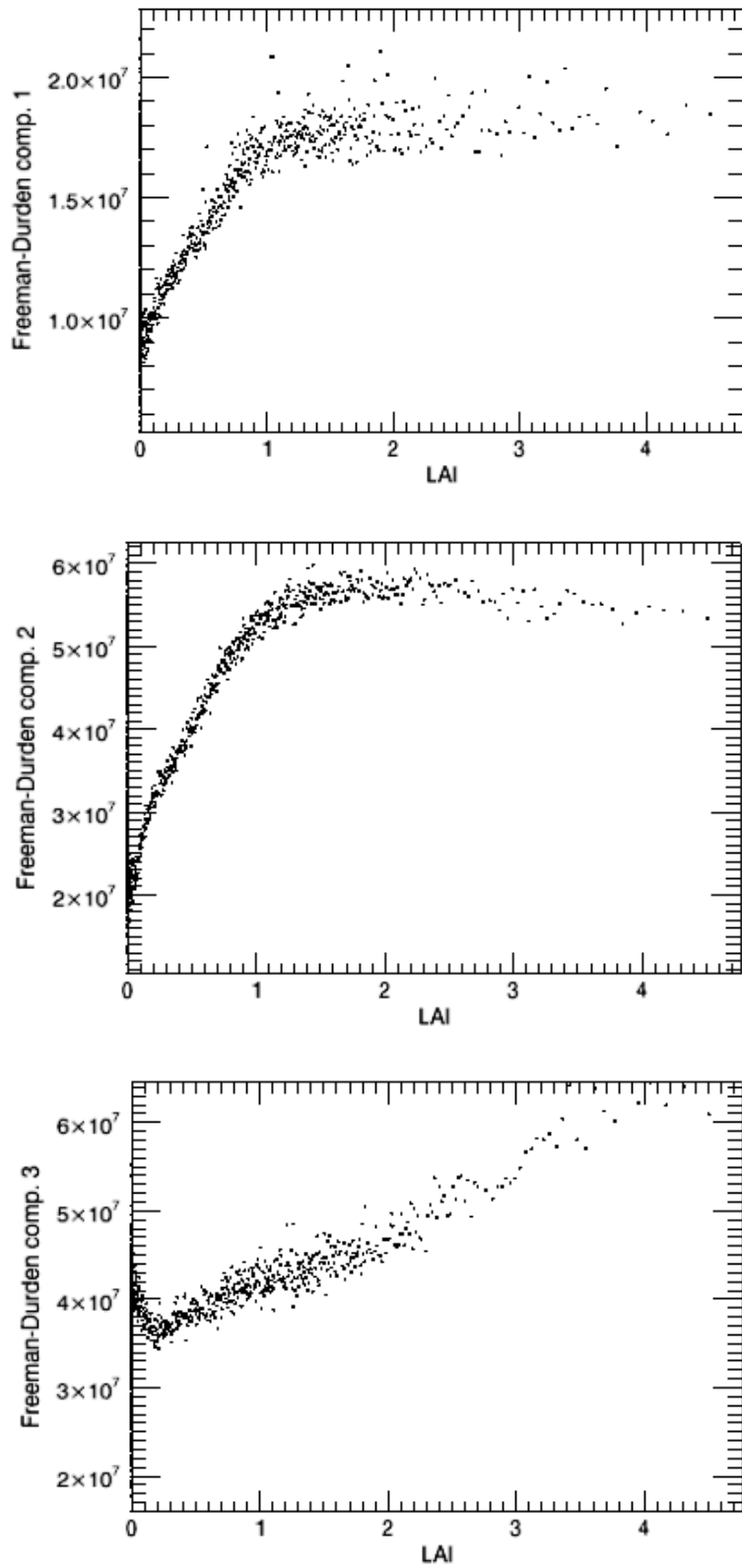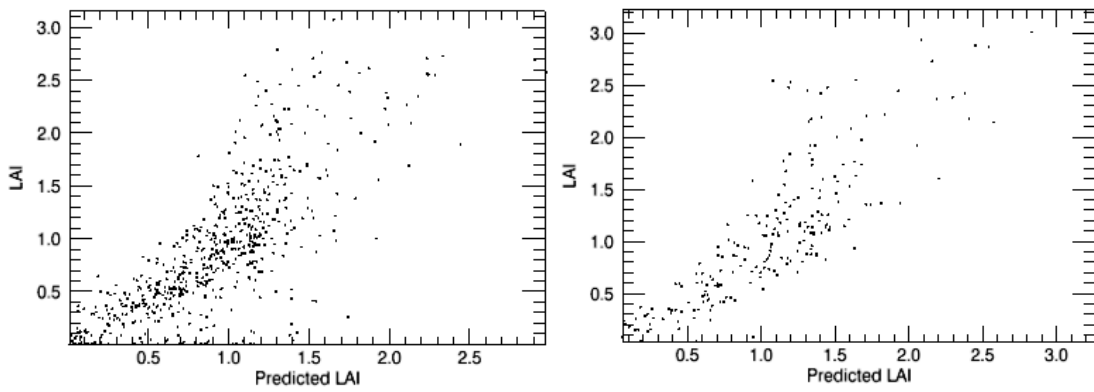
Figure 22: LAI versus predicted LAI using Method 1 (left) and Method 3 (right) on the Freeman-Durden components of the R2 image of Sept. 3, 2008 and the quadratic model. The coefficient of determination were $R^2=0.58$ (MSE=0,17) and 0.70 (MSE=0.13), respectively.

The results for the July 24 and Sept. 27 scenes were worse than for the Sept. 3 scene (Tab. 3). The pixel-wise correspondence (1 sample) resulted is a poor fit (Tab.3), and increasing the number of samples in each LAI cell (288 samples) did not improve the estimation results (Tab. 3). As for ENVISAT ASAR, the backscatter ratio VV/HH was not suitable for estimating the LAI, and the coefficient of determination were for all scenes less than 0.07 (Tab. 3)!

The PC90 data correlated a little higher for the XX-channel ($R^2=0.67$), and little less for the HH- and VV-channels ($R^2=0.55$, $R^2=0.57$) (Tab. 4).

The individual Freeman-Durden components were evaluated for estimating LAI and PC90. For both LAI and PC90, the volume scatter component was the best one (Tabs. 3 and 4). Whereas the surface scatter component provided the worse fit. In fact, for PC90 the R^2 –value was only 0.08.

4.2.2 Summary LAI estimation using Radarsat-2

Table 3: Summary of LAI estimation results using Radarsat-2

Scene	Model	Method 1		Method 3	
		R-sq	MSE	R-sq	MSE
R2 – Sep. ,3	a0 + a1*HH	0.50	0.21	0.60	0.18
	a0 + a1*XX	0.44	0.23	0.50	0.22
	a0 + a1*VV	0.50	0.21	0.67	0.15
	a0 + a1*HH + a2*HH^2 + a3*VV +a4*VV^2	0.60	0.17	0.72	0.12
	a0 + a1*(VV/HH)			0.014	0.46
	a0 + a1*P1	0.39	0.25	0.44	0.25
	a0 + a1*P1	0.41	0.25	0.48	0.23
	a0 + a1*P3	0.33	0.28	0.59	0.19
	a0 + a1*P1 + a2*P1^2 + a3*P2 +a4*P2^2 + a5*P3 +a6*P3^2	0.56	0.18	0.70	0.13
	a0+a1*FD2 (double bounce)	0.35	0.27	0.40	0.27
	a0+a1*FD2 (volume scatter)	0.43	0.24	0.48	0.33
	a0+a1*FD2 (single bounce/surface)	0.22	0.33	0.31	0.32
	a0 + a1*FD1 + a2*FD1^2 + a3*FD2 +a4*FD2^2 + a5*FD3 +a6*FD3^2	0.59	0.17	0.71	0.13
R2 -- July, 17	a0 + a1*HH	0.27	0.31	0.35	0.30
	a0 + a1*XX	0.40	0.25	0.48	0.23
	a0 + a1*VV	0.31	0.29	0.45	0.25
	a0 + a1*(VV/HH)			0.068	0.43
R2 – Sep., 27	a0 + a1*HH	0.08	0.39	0.02	0.45
	a0 + a1*XX	0.30	0.30	0.32	0.30

	a0 + a1*VV	0.13	0.37	0.19	0.38
	a0 + a1*(VV/HH)			0.011	0.41
R2 – Sep. ,3 288 samples	a0 + a1*HH	0.52	0.16	0.62	0.11
	a0 + a1*XX	0.44	0.19	0.67	0.095
	a0 + a1*VV	0.54	0.16	0.65	0.11
R2 – Sep. ,3 1 sample	a0 + a1*HH	0.062	0.72	-	-
	a0 + a1*XX	0.10	0.69	-	-
	a0 + a1*VV	0.075	0.71	-	-

4.2.3 Summary PC90 estimation using Radarsat-2

Table 4: Summary of PC90 estimation results using Radarsat-2.

Scene	Model	Method 3	
		R-sq	MSE
R2 – Sep. ,3	a0 + a1*HH	0.55	8.1
	a0 + a1*XX	0.67	5.8
	a0 + a1*VV	0.57	8.0
	$a0 + a1*HH + a2*HH^2 + a3*VV + a4*VV^2$	0.72	5.1
	a0 + a1*P1	0.63	6.5
	a0 + a1*P1	0.63	6.5
	a0 + a1*P3	0.43	10.6
	$a0 + a1*P1 + a2*P1^2 + a3*P2 + a4*P2^2 + a5*P3 + a6*P3^2$	0.71	5.4
	a0 + a1*FD1 (double bounce)	0.60	7.31

	a0 + a1*FD2 (volume)	0.67	5.84
	a0 + a1*FD3 (single bounce/surface)	0.082	17.3
	a0 + a1*FD1 + a2*FD1^2 + a3*FD2 +a4*FD2^2 + a5*FD3 +a6*FD3^2	0.72	5.0

5 Discussions and conclusion

In this work we have estimated the LAI from C-band ENVISAT ASAR Alternating polarization and Radarsat-2 Fine-Quad polarization SAR data and compared the results to LAI retrieved from airborne LIDAR, which were regarded as "ground truth".

Analyses of the backscatter (Method 2) revealed that the radar backscatter correlated strongly with LAI for small values of LAI, but saturated for LAI values above 1 - 2. However, the 3rd component (single bounce) of the Freeman-Durden decomposition showed a linear trend for LAI values above 0.3, and the VV-channel was increasing for increasing LAI values. None of these covariates saturated for LAI values below 4. Similar behavior of the radar backscatter from corn, sorghum and wheat was established by Ulaby et al. (1984) where also the backscatter saturated for LAI values above a certain value. Saturation of the radar backscatter was also observed when compared to biomass (Dobson et al., 1992). It is expected that the LAI saturation level is dependent of the radar frequency, as it was established for biomass (Dobson et al, 1992). The analyses of the Method-2 scatter plots (Figs. 9, 14, 18 and 21), indicated an upper bound of how good the LAI may be estimated from the radar data. Thus, it is not expected that Method 1 (block averaging) or 3 (averaging of homogeneous segments) would perform better than Method 2.

Method 3 was in general better than Method 1 for both ENVISAT ASAR (Tab. 1) and Radarsat-2 (Tab. 3), indicating that the LAI values within a segment were more homogeneous than within a square block. However, some uncertainties remain since the segments are constructed from the LIDAR data. It is unclear how the performance would be if the segments were constructed from a forest abundance map. Radarsat-2 data provided much better correspondence against LAI than ENVISAT ASAR data, with a coefficient of determination as high as 0.72 for the quadratic model (Fig. 16 and Tab. 3). However, the VV-channels performed nearly as well (R^2=0.67), which may be explained that it does not saturate (Fig. 14, lower panel and Fig. 15, lower-right). We were not able to reproduce the extremely good LAI predictions obtained by Manninen et al. (2005), and the backscatter VV/HH ratio was the covariate that we obtained the worst fit against LAI with for both ENVISAT ASAR and Radarsat-2. The reason for this in unclear, but may be related to the careful selection of forest areas done in the work by Manninen et al. (2005).

The ability to predict the LAI varied substantially between the images. For instance, for Radarsat-2 Sept. 3, we obtained an R^2=0.60 for the HH-channel but this was R^2=0.35 for July 17, and equal to 0 for the Sept. 27 scene. We expect that this variation is related to factors such as soil and vegetation moisture content. However, no in situ measurements are available to verify this.

There exist a few models of the backscatter as a function of LAI for forest vegetation. These models are in general very complex, and an inverse function (i.e. a function describing LAI as a function of radar backscatter) is more or less impossible to obtain (Freeman and Durden, 1994). We have in this work focused on using a simple quadratic model to predict the LAI from the backscatter measurements. We have also investigated Generalized Linear Models, but they did not, in general, provide better fits.

The backscatter need to be averaged in order to provide usable estimation of the LAI. Comparing the pixel-wise correspondence between LAI and the backscatter resulted in low R^2 values (Tab.3, 20x20m, 1 sample). Regarding the resolution of the LAI cells, 240x240m (144 samples) (similar as Manninen et al. (2005)) seemed to be a good choice for these data. We explored lower resolution (480x480m, 288 samples) but we did not observe any better LAI prediction (Tab. 1 and 3).

The ability to predict PC90 measurements (Tab. 2 and 4) from radar was found to be similar to predicting LAI. Also here Radarsat-2 gave better results than ENVISAT ASAR. Interestingly, we obtained the best fit to the PC90 using the XX-component of the Radarsat-2 data.

For the limited study of the LAI estimation using ENVISAT ASAR and Radarsat-2 data we conclude that Radarsat-2 data were much better for LAI estimation than ENVISAT ASAR data. The VV-channel is the most suitable covariate to use, and for Radarsat-2 the VV-component performed nearly equally well as the quadratic model with 6 covariates. We also recommend that several SAR images are required from the sensor since the estimation results varied considerably between the images, and that the LAI values are low or moderate.

6 References

Dobson, M. C., Ulaby, F. T., LeToan, T., Beaudoin, A., Kaisichke, E. S., and Christensen, N. (1992), "Dependence of radar backscatter on coniferous forest biomass", *IEEE Trans. Geosci. Remote Sens.,* vol. 30, no. 2, pp. 412—415.

Durden, S. L., van Zyl, J. J., and Zebker, H. A. (1989), "Modeling and observation of the radar polarization signature of forested areas", *IEEE Trans. Geosci. Remote Sens.*, vol. 27, no. 3, pp.290—301.

Durden, S. L., Morrissey, L. A., and Livingston, G. P. (1995), "Microwave backscatter and attenuation dependence on leaf area index for flooded rice fields", *IEEE Trans. Geosci. Remote Sens.* vol 33, no. 3, pp.807—810.

Freeman, A. and Durden, S. L. (1998), "A three-component scattering model for polarimetric SAR data", *IEEE Trans. Geosci. Remote Sens.*, vol 36, no. 3.

Karam, M. A., Fung, A. K., Lang, R. H., and Chauhan, N. S. (1992), "A microwave scattering modell for layered vegetation", *IEEE Trans. Geosci. Remote Sens.* Vol. 30, no. 4.

Leckie, D. G. and Ranson, K. J. (1998), "Forestry applications using imaging radar", in "Principle and Applications of Imaging Radar. Manual of Remote Sensing", 3rd Ed, Vol. 2, Wiley, New York.

Manninen, T., Stenberg, P., Rautiainen, M., Voipio P., and Smolander, H. (2005), "Leaf area index estimation of boreal forest using ENVISAT ASAR*", IEEE Trans. Geosci. Remote Sens.*, vol 43, no. 11, pp. 2627—2635.

Solberg, S., Brunner, A., Hanssen, K. H., Lange, H., Næsset, E., Rautiainen, M., and Stenberg, P. (2009), "Mapping LAI in a Norway spruce forest using airborne laser scanning", *Remote Sensing of Environment*, vol. 113, no. 11, pp. 2317—2327.

Ulaby, F. T., Allen, C. T., and Eger III, G. (1984), "Relating the microwave backscattering coefficient to leaf area index", *Remote Sensing of Environment*, vol. 14, pp. 113—133.

Ulaby, F. T., Sarabandi, K., McDonal, K. C., Whitt, M. W., and Dobson, M. C. (1990), "Michigan microwave canopy scattering model", *Int. J. Remote Sensing*, vol. 11, no. 7, 1223—1253.

Woodhouse, I. H. (2006), "Introduction to Microwave Remote Sensing", Tayor and Francis, Boca Raton, Fl.

Zheng, G., and Moskal, L. M. (2009), "Retrieving the leaf area index (LAI) using remote sensing: Theories, methods and sensors", *Sensors*, vol. 9, pp. 2719—2745.